

# Coupling non-matching finite element discretizations in small-deformation inelasticity: Numerical integration of interface variables

Layla K. Amaireh<sup>1</sup> and Ghadir Haikal<sup>\*2</sup>

<sup>1</sup>Applied Science Private University, Amman, Jordan

<sup>2</sup>Lyles School of Civil Engineering, Purdue University, West Lafayette, Indiana, USA

(Received August 4, 2018, Revised September 6, 2018, Accepted September 7, 2018)

**Abstract.** Finite element simulations of solid mechanics problems often involve the use of Non-Conforming Meshes (NCM) to increase accuracy in capturing nonlinear behavior, including damage and plasticity, in part of a solid domain without an undue increase in computational costs. In the presence of material nonlinearity and plasticity, higher-order variables are often needed to capture nonlinear behavior and material history on non-conforming interfaces. The most popular formulations for coupling non-conforming meshes are dual methods that involve the interpolation of a traction field on the interface. These methods are subject to the Ladyzhenskaya-Babuska-Brezzi (LBB) stability condition, and are therefore limited in their implementation with the higher-order elements needed to capture nonlinear material behavior. Alternatively, the enriched discontinuous Galerkin approach (EDGA) (Haikal and Hjelmstad 2010) is a primal method that provides higher order kinematic fields on the interface, and in which interface tractions are computed from local finite element estimates, therefore facilitating its implementation with nonlinear material models. The inclusion of higher-order interface variables, however, presents the issue of preserving material history at integration points when a increase in integration order is needed.

In this study, the enriched discontinuous Galerkin approach (EDGA) is extended to the case of small-deformation plasticity. An interface-driven Gauss-Kronrod integration rule is proposed to enable adaptive enrichment on the interface while preserving history-dependent material data at existing integration points. The method is implemented using classical J2 plasticity theory as well as the pressure-dependent Drucker-Prager material model. We show that an efficient treatment of interface variables can improve algorithmic performance and provide a consistent approach for coupling non-conforming meshes in inelasticity.

**Keywords:** non-conforming mesh coupling; the enriched discontinuous Galerkin method; J2 plasticity; drucker-prager model; numerical integration

## 1. Introduction

With the advent of powerful computing, the Finite Element Method (FEM) has become a popular tool for simulating many complex engineering problems with a high level of detail. Finite element models have been successfully used to predict the behavior of large-scale systems under

---

\*Corresponding author, Assistant Professor, E-mail: [ghaikal@purdue.edu](mailto:ghaikal@purdue.edu)

extreme events, in which failure mechanisms such as fracture, damage and inelasticity can be captured using advanced nonlinear material models. To ensure the accuracy of the simulation, however, a high level of mesh refinement is needed at locations of material nonlinearity, often requiring the use of higher-order (quadratic and above) elements. Therefore, in order to minimize computational cost while maintaining accuracy at potential failure locations, it has become customary to use different levels of mesh refinement within the finite element model, creating a *Non-Conforming Mesh* (NCM) discretization and introducing artificial interfaces between domains with different levels of mesh refinement.

A finite element mesh is denoted non-conforming when  $C^0$  continuity of the displacement field no longer holds along interfaces between elements. This occurs in contact and coupled problems due to the presence of a physical interface, and, generally, in discretizations where element nodes do not coincide. The main challenge in modeling non-conforming meshes is to ensure deformation compatibility and continuity of interface tractions in the absence of full displacement continuity along element interfaces. In the presence of nonlinear effects such as inelasticity, it is crucial for the model to transfer geometric and material gradients, as well as history-dependent material variables, accurately across the numerical interface.

Previous studies have proposed different techniques to resolve the challenge of enforcing interface conditions in NCMs, and available methods can be grouped in the general categories of primal and dual approaches. The distinction between these two families of methods is in the type of the interface variables. While primal methods retain the displacement-based nature of the finite element discretizations, dual methods employ a field of Lagrange multipliers, representing tractions, on the interface to enforce weak geometric compatibility constraints. The Lagrange multipliers at the nodes along one side of the interface, called “slave” are computed from the interpolated dual field based on the other side of the interface, designated “master.” Dual methods therefore satisfy the continuity of interface tractions, typically reflected in the standard patch test, by design. The choice of the Lagrange multiplier interpolation field, however, is restricted by the Ladyzhenskaya-Babuška-Brezzi (LBB) condition that governs the stability of dual finite element discretizations (Brezzi and Fortin 1991). Furthermore, the master/slave designation is not always trivial and introduces a bias in the result.

The most popular dual formulation is the mortar family of methods, originally proposed by Bernardi *et al.* (1992), and others (Le Tallec *et al.* 1995). This approach was also applied to contact problems, first by Belgacem *et al.* (1999), and later by Puso and Laursen (2004), Fischer and Wriggers (2005), and Dickopf and Krause (2009). To avoid sensitivity to the master/slave designation, dual mortar methods were also proposed by Wohlmuth (2000), Solberg and Papadopoulos (2005), and Solberg *et al.* (2007), both for coupling non-conforming meshes and for the contact problem, where tractions fields are interpolated on both sides of the interface. Mortar methods have enjoyed great popularity in the literature on contact and coupled problems, and the above seminal works were among the first of numerous applications of mortar formulations. Despite their success, mortar formulations have been limited by stability requirements that restrict the order of interpolation for the dual fields. Consequently, despite early successes in nonlinear problems undergoing large deformations (Yang *et al.* 2005), the application of mortar methods to plasticity have been somewhat limited. A comprehensive study of mortar methods by Popp and Wall (2014) discusses many issues pertaining to numerical integration and the use of higher-order elements for nonlinear material modeling. Other dual approaches include the class of Finite Element Tearing and Interconnecting (FETI) domain decomposition methods based on the work of Farhat (1991) (see Farhat *et al.* (2007), Bavestrello *et al.* (2007), Bernardi *et al.* (2008) and

Bernardi *et al.* (2009) for a non-inclusive list), which suffer similar restrictions. The LBB condition can be relaxed using a stabilization procedure in which the kinematic field within the element is enhanced with higher-order functions. Works based on this approach include numerous formulations that employ the eXtended Finite Element (Dolbow and Harari 2009), and variational multiscale (Masud *et al.* 2012) methods.

In primal methods, the interface is represented by its displacement fields; therefore, these approaches are not subject to the LBB restrictions. A number of primal formulations have been proposed for contact and coupled problems, the most popular of which are based on the Discontinuous Galerkin (DG) framework and the Nitsche (1971) approach for enforcing kinematic constraints. The Discontinuous Galerkin (DG) methodology is natural to non-conforming mesh discretizations since it readily assumes discontinuous discretizations on all inter-element interfaces. DG formulations are based on identifying a set of target continuous displacement and traction fields on each interface, and mapping the discretized displacement and traction variables on each surface to these target fields, or numerical fluxes, in a weak weighted residual form. A good survey of these methods can be found in Arnold *et al.* (2002). The Nitsche method (Nitsche 1971) is a consistent primal formulation that employs a penalty approach to enforcing kinematic conditions. Originally introduced for the treatment of rough Dirichlet boundaries, this method was applied to the coupling of nonconforming meshes by Hansbo and Hansbo (2002) and Becker *et al.* (2003). The Nitsche method has also been used as a basis for developing primal stabilized interface formulations for embedded interfaces (Riviere *et al.* 1999, Dolbow and Harari 2008, Sanders *et al.* 2009). Other primal interface formulations include the Interface Element Method introduced by Kim (2002, 2003), which has recently been applied to contact problems with inelasticity (Jin *et al.* 2015).

Primal methods, in general, are challenged by the task of enforcing both geometric compatibility and continuity of the tractions using a primal variable field. As a result, primal methods often require a mesh-dependent stabilization parameter to ensure the convergence of the solution in the limit of mesh refinement. The properties of stability and convergence, however, can only be guaranteed for linear problems. Hybrid methods employ non-conforming discretizations within the Discontinuous Galerkin method, while providing additional degrees of freedom on the skeleton of the mesh that can be condensed at the element level. These methods have recently gained popularity (Bayat *et al.* 2018), but have been mostly applied to linear elasticity (Hansbo and Larson 2016, Wihler 2006, Liu *et al.* 2009, Di Pietro and Nicaise 2013, Grieshaber *et al.* 2015), with few extensions to plasticity (Liu *et al.* 2013). Other specialized primal elements such as the nonconforming formulation of Bitencourt *et al.* (2015), the Virtual Element Method (Wriggers *et al.* 2016), the Domain Interface Method (DIM) (Lloberas-Valls *et al.* 2017), and the mid-edge tetrahedron (Hansbo, and Larsson, 2016), modify the standard Galerkin formulation, therefore increasing the complexity and associated computational cost of the finite element numerical solution.

Haikal and Hjelmstad (2010) proposed a stabilized primal interface formulation that employs a local enrichment of primary interface variables to transform kinematic compatibility conditions to node-to-node constraints applied on both sides of the interface. This approach enables an unbiased enforcement of kinematic compatibility constraints and is shown to eliminate surface locking. To guarantee a complete transfer of forces along the interface, the method implements a stabilization procedure based on the Discontinuous Galerkin method, in which the stabilization terms enforce a weak equilibrium of interface tractions. This method can be classified as hybrid approach in which interface tractions are obtained from direct estimates of stress fields on the interface, without the

need for dual interpolations or mesh-dependent parameters. The stabilization terms are in fact derived from the continuum coupled problem and vanish when the meshes match along the interface. This method, therefore, includes the standard Galerkin method as a subset. The displacement compatibility constraints are enforced strongly at the nodes using Lagrange multipliers and therefore no regularization is needed for either the displacement gap or pressure across the interface. The method has been successfully used in small and large deformations solid mechanics formulations, as well as for the coupling of beam and solid finite element discretizations (Montero and Haikal 2018).

Simulating the nonlinear behavior of coupled problems involves high deformation gradients and material degradation on interfaces connecting different physical domains and/or numerical discretizations. These phenomena are difficult to capture adequately within the standard finite element method due to the low accuracy of strain and stress fields on these interfaces. Solution accuracy can be improved using higher-order interpolations for interface flux and deformation fields. To incorporate interface-targeted refined discretizations, however, available methods require a significant modification to the underlying finite element formulation. Furthermore, the inclusion of higher-order interface variables increases the numerical cost associated with modeling nonlinear interfacial effects, particularly in the presence of material and geometric nonlinearities. Most available implementations of non-conforming mesh coupling formulations have been developed and applied in the realm of linear elasticity. Extensions to nonlinear analysis have been limited by mesh sensitivity in penalty-type stabilizations and difficulties for primal methods, and LBB restrictions for dual methods.

This work proposes an effective approach for capturing high-order material nonlinearities on interfaces that balances the requirements of accuracy and algorithmic efficiency. The proposed method is an extension of the Enriched Discontinuous Galerkin Approach (EDGA) introduced by Haikal and Hjelmstad (2010), which implements an element-level surface enrichment along with an interface stabilization procedure based on the Discontinuous Galerkin formulation to enable a two-pass approach for enforcing strong geometric compatibility conditions while ensuring weak continuity of surface tractions. Traction fields are obtained directly from finite element estimates on the interface, a feature that facilitates the implementation of inelastic material laws in a manner that is consistent with element formulation away from the interface. An interface-driven Gauss-Kronrod integration rule is proposed to enable adaptive enrichment on the interface while preserving history-dependent material data at existing integration points. It is shown that an efficient treatment of interface variables can improve algorithmic performance and circumvent numerical issues encountered in the presence of nonlinear material behavior.

The outline of the paper is as follows: Section 2 summarizes the formulation of the coupled problem for linear elasticity and the Enriched Discontinuous Galerkin Approach (EDGA) is outlined in Section 3. Section 4 overviews the material models used in this study, while Section 5 discusses the numerical integration procedure needed for the implementation of the EDGA for history-dependent materials. Numerical examples are discussed in Section 6, and conclusions are summarized in Section 7.

## 2. Formulation

Consider the two solid domains  $\Omega^1$  and  $\Omega^2$  meeting through a non-conforming interface  $\Gamma_*$  as shown in Fig. 1. The boundary  $\Gamma$  of each domain can be divided into three parts  $\Gamma = \Gamma_t \cup \Gamma_u \cup \Gamma_*$ ,

where  $\Gamma_t$  and  $\Gamma_u$  denote the Neumann and Dirichlet parts of that boundary, respectively. Note that  $\Gamma_t \cap \Gamma_u \cap \Gamma_* = \emptyset$  in each body.

Given the body force vector field for each solid  $\mathbf{b}^1$  and  $\mathbf{b}^2$ , a prescribed traction  $\mathbf{t}^1$  and  $\mathbf{t}^2$  on  $\Gamma_t^1$  and  $\Gamma_t^2$ , respectively, and a prescribed displacement field  $\mathbf{g}^1$  and  $\mathbf{g}^2$  on  $\Gamma_u^1$  and  $\Gamma_u^2$ , the strong form of the governing equations of the coupled problem can be written as follows

$$\begin{aligned} \operatorname{div} \boldsymbol{\sigma}^1 + \mathbf{b}^1 &= \mathbf{0} \text{ in } \Omega^1, \boldsymbol{\sigma}^1 \mathbf{n}^1 = \mathbf{t}^1 \text{ on } \Gamma_t^1, \mathbf{u}^1 = \mathbf{g}^1 \text{ on } \Gamma_u^1 \\ \operatorname{div} \boldsymbol{\sigma}^2 + \mathbf{b}^2 &= \mathbf{0} \text{ in } \Omega^2, \boldsymbol{\sigma}^2 \mathbf{n}^2 = \mathbf{t}^2 \text{ on } \Gamma_t^2, \mathbf{u}^2 = \mathbf{g}^2 \text{ on } \Gamma_u^2 \end{aligned} \quad (1)$$

in addition to compatibility conditions on the interface

$$\mathbf{u}^1 = \mathbf{u}^2, \quad \mathbf{t}^1 + \mathbf{t}^2 = \mathbf{0} \text{ on } \Gamma_*. \quad (2)$$

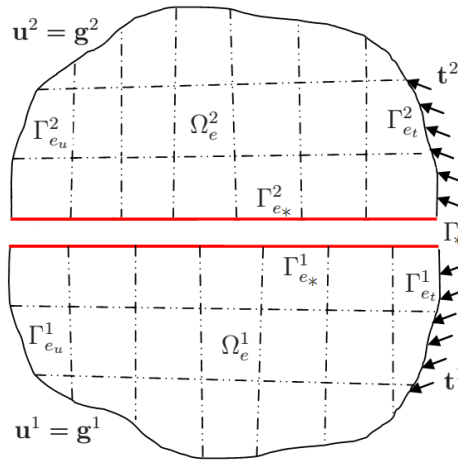


Fig. 1 Two solid domains in non-conforming discretizations

In these equations,  $\boldsymbol{\sigma}$  is the Cauchy stress tensor,  $\operatorname{div}$  is the divergence operator and  $\mathbf{n}$  is the normal to the domain surface. Defining the subspaces  $V^i = \{\mathbf{w}^i \in H^1(\Omega^i): \mathbf{w}^i = \mathbf{0} \text{ on } \Gamma_u^i\}$  in each domain  $i$ , we can express the weighted residual form of the governing equations as follows

$$\int_{\Omega^i} [\operatorname{div} \boldsymbol{\sigma}^i + \mathbf{b}^i] \cdot \mathbf{w}^i d\Omega + \int_{\Gamma_t^i} [\mathbf{t}^i - \boldsymbol{\sigma}^i \mathbf{n}^i] \cdot \mathbf{w}^i d\Gamma = 0 \quad \forall \mathbf{w}^i \in V^i, i = 1,2 \quad (3)$$

Now consider a discretization of each domain into a set of finite elements such that  $\Omega^i = \sum_e \Omega_e^i, i = 1,2$ , as shown in Fig. 1. Note that the discretizations do not necessarily produce matching nodes on the interface, and as such the displacement field is not point-wise continuous on  $\Gamma_*$ . The element surfaces that are part of the domain Neumann boundary in each domain are denoted  $\Gamma_{e_t}^1, \Gamma_{e_t}^2$ , while the Dirichlet element boundaries are referred to as  $\Gamma_{e_u}^1, \Gamma_{e_u}^2$ . Element surfaces along the interface between the two domains are designated as  $\Gamma_{e_*}^1, \Gamma_{e_*}^2$ . To wit,

$$\begin{aligned} \Gamma_e^i &= \Gamma_{e_t}^i \cup \Gamma_{e_u}^i \cup \Gamma_{e_*}^i \\ \Gamma_{e_t}^i \cap \Gamma_{e_u}^i &= \Gamma_{e_t}^i \cap \Gamma_{e_*}^i = \Gamma_{e_*}^i \cap \Gamma_{e_u}^i = \emptyset, i = 1,2 \end{aligned}$$

The discretized form of the weighted residual in each domain is, therefore,

$$\sum_e^i \int_{\Omega_e^i} [\text{div } \boldsymbol{\sigma}^{ih} + \mathbf{b}^i] \cdot \mathbf{w}^{ih} d\Omega + \sum_e^i \int_{\Gamma_{e_t}^i} [\mathbf{t}^i - \boldsymbol{\sigma}^{ih} \mathbf{n}^i] \cdot \mathbf{w}^{ih} d\Gamma = 0 \quad \forall \mathbf{w}^i \in V^i, i = 1, 2 \quad (4)$$

We now apply the divergence theorem to the first term in Eq. (4), and enforce homogeneous boundary conditions on the variational fields to find the symmetric weighted residual, or virtual work, forms in each body as

$$\begin{aligned} & - \sum_e^i \int_{\Omega_e^i} \boldsymbol{\sigma}^{ih} \cdot \nabla \mathbf{w}^{ih} d\Omega + \sum_e^i \int_{\Omega_e^i} \mathbf{b}^i \cdot \mathbf{w}^{ih} d\Omega + \sum_e^i \int_{\Gamma_{e_t}^i} \mathbf{t}^i \cdot \mathbf{w}^{ih} d\Gamma \\ & + \sum_e^i \int_{\Gamma_{e_*}^i} \boldsymbol{\sigma}^{ih} \mathbf{n}^i \cdot \mathbf{w}^{ih} d\Gamma = 0 \quad \forall \mathbf{w}^i \in V^i, i = 1, 2. \end{aligned} \quad (5)$$

The combined virtual work form in the coupled system can therefore be expressed as follows

$$\begin{aligned} & - \sum_e^1 \int_{\Omega_e^1} \boldsymbol{\sigma}^{1h} \cdot \nabla \mathbf{w}^{1h} d\Omega + \sum_e^1 \int_{\Omega_e^1} \mathbf{b}^1 \cdot \mathbf{w}^{1h} d\Omega + \sum_e^1 \int_{\Gamma_{e_t}^1} \mathbf{t}^1 \cdot \mathbf{w}^{1h} d\Gamma \\ & - \sum_e^2 \int_{\Omega_e^2} \boldsymbol{\sigma}^{2h} \cdot \nabla \mathbf{w}^{2h} d\Omega + \sum_e^2 \int_{\Omega_e^2} \mathbf{b}^2 \cdot \mathbf{w}^{2h} d\Omega + \sum_e^2 \int_{\Gamma_{e_t}^2} \mathbf{t}^2 \cdot \mathbf{w}^{2h} d\Gamma \\ & + \sum_e^1 \int_{\Gamma_{e_*}^1} \boldsymbol{\sigma}^{1h} \mathbf{n}^1 \cdot \mathbf{w}^{1h} d\Gamma + \sum_e^2 \int_{\Gamma_{e_*}^2} \boldsymbol{\sigma}^{2h} \mathbf{n}^2 \cdot \mathbf{w}^{2h} d\Gamma = 0 \quad \forall \mathbf{w}^i \in V^i, i = 1, 2. \end{aligned} \quad (6)$$

The first six terms in Eq. (6) constitute the virtual work forms of the statement of equilibrium within the two domains, while the last two terms represent the work of surface tractions along the two sides of the non-conforming interface. Noting that  $\mathbf{n}^1 = -\mathbf{n}^2 = \mathbf{n}^*$ , we observe that when both sides are discretized with a set of conforming elements  $\Gamma_* = \sum_{e_*} \Gamma_{e_*}$ ,  $\mathbf{w}^{1h} = \mathbf{w}^{2h} = \mathbf{w}^{*h}$  the interface terms reduce to

$$\sum_e^1 \int_{\Gamma_{e_*}^1} \boldsymbol{\sigma}^{1h} \mathbf{n}^1 \cdot \mathbf{w}^{1h} d\Gamma + \sum_e^2 \int_{\Gamma_{e_*}^2} \boldsymbol{\sigma}^{2h} \mathbf{n}^2 \cdot \mathbf{w}^{2h} d\Gamma = \sum_{e_*} \int_{\Gamma_{e_*}} [\boldsymbol{\sigma}^{1h} - \boldsymbol{\sigma}^{2h}] \mathbf{n}^* \cdot \mathbf{w}^{*h} d\Gamma, \quad (7)$$

which is a weak enforcement of equilibrium or tractions on the interface between the two bodies.

The above result underscores the importance of the displacement discretization in enforcing interface conditions. In the standard Bubnov-Galerkin finite element formulation, real and variational displacement fields are interpolated similarly, and displacement continuity naturally implies traction balance on element interfaces. Assuming conforming discretizations within each domain, the weighted residual form of the governing equations for the coupled problem can be stated as

$$\begin{aligned} & - \sum_e^1 \int_{\Omega_e^1} \boldsymbol{\sigma}^{1h} \cdot \nabla \mathbf{w}^{1h} d\Omega + \sum_e^1 \int_{\Omega_e^1} \mathbf{b}^1 \cdot \mathbf{w}^{1h} d\Omega + \sum_e^1 \int_{\Gamma_{e_t}^1} \mathbf{t}^1 \cdot \mathbf{w}^{1h} d\Gamma \\ & - \sum_e^2 \int_{\Omega_e^2} \boldsymbol{\sigma}^{2h} \cdot \nabla \mathbf{w}^{2h} d\Omega + \sum_e^2 \int_{\Omega_e^2} \mathbf{b}^2 \cdot \mathbf{w}^{2h} d\Omega + \sum_e^2 \int_{\Gamma_{e_t}^2} \mathbf{t}^2 \cdot \mathbf{w}^{2h} d\Gamma + I_* = 0 \end{aligned} \quad (8)$$

$$I_* = \sum_e^1 \int_{\Gamma_{e_*}^1} \boldsymbol{\sigma}^{1h} \mathbf{n}^1 \cdot \mathbf{w}^{1h} d\Gamma + \sum_e^2 \int_{\Gamma_{e_*}^2} \boldsymbol{\sigma}^{2h} \mathbf{n}^2 \cdot \mathbf{w}^{2h} d\Gamma \quad (9)$$

The goal of any coupling scheme is to enforce displacement compatibility and equilibrium of interface traction fields such that  $I_* = 0$ .

### 3. Interface model: EDGA

The Enriched Discontinuous Galerkin Approach (EDGA) (Haikal and Hjelmstad 2010) seeks to solve the continuity problem at the interface of NCMs by enforcing strong displacement continuity at interface nodes, while ensuring balance of tractions along interface elements. The EDGA is a primal approach that enables a two-pass strategy for the enforcement of geometric compatibility conditions through a local enrichment designed to guarantee geometric compatibility at all nodes of the interface, without the need of a master-slave definition. The local enrichment transforms the geometric compatibility condition to a set of node-to-node constraints by inserting a new node at locations where a node on one side of the interface meets an element surface on the other. Completeness of the finite element interpolation in the enriched element is preserved by updating the set of Lagrangian shape functions to account for the additional node. Since the displacement between the nodes remains discontinuous, a Discontinuous Galerkin (DG) stabilization is applied to weakly enforce the continuity of tractions along the interface. The EDGA is summarized below (Haikal and Hjelmstad 2010).

#### 3.1 EDGA: Surface enrichment

Consider the non-matching finite element configuration shown in Fig. 2(a). When a node  $p$  meets the top surface 34 of an element 1234, a node 5 is inserted on the element surface at the location of  $p$ , and a shape function corresponding to the inserted node 5 is defined, such that as illustrated in Fig. 2(a).

$$\tilde{N}^5(\boldsymbol{\zeta}, \boldsymbol{\zeta}^p) = \frac{1}{2}(\zeta_2 + 1) \frac{(\zeta_1 + 1)(\zeta_1 - 1)}{(\zeta_1^p + 1)(\zeta_1^p - 1)} \quad (10)$$

where  $\boldsymbol{\zeta} = (\zeta_1, \zeta_2)$  are the element parent coordinates and  $\boldsymbol{\zeta}^p = (\zeta_1^p, 1)$  denotes the projection of  $p$  onto the element parent domain. To preserve the interpolatory nature of the finite element basis and its partition of unity property, the shape functions associated with existing nodes are modified as follows

$$\tilde{N}^\alpha(\boldsymbol{\zeta}, \boldsymbol{\zeta}^p) = N_{Q4}^\alpha(\boldsymbol{\zeta}) - N_{Q4}^\alpha(\boldsymbol{\zeta}^p) \tilde{N}^5(\boldsymbol{\zeta}, \boldsymbol{\zeta}^p) \quad (11)$$

In this equation,  $\tilde{N}^\alpha(\boldsymbol{\zeta}, \boldsymbol{\zeta}^p)$  are the modified (enriched) element shape functions,  $\tilde{N}^5(\boldsymbol{\zeta}, \boldsymbol{\zeta}^p)$  is the shape function of the enriched node (Eq. 10),  $N_{Q4}^\alpha(\boldsymbol{\zeta})$  is the shape function of a Q4 element for  $\alpha = 1, \dots, 4$ ,

$$N_{Q4}^\alpha(\boldsymbol{\zeta}) = \frac{1}{4}(\zeta_1 \pm 1)(\zeta_2 \pm 1) \quad (12)$$

The spatial coordinates of the additional node corresponds to that of node  $p$ , and compatibility conditions can be imposed discretely at enrichment locations ( $\mathbf{u}^p = \mathbf{u}^5$ ). This procedure can be repeated with multiple nodes for a given element, as shown in Fig. 2(b), and enrichments are added on both sides of the interface. Each added node provides additional degrees of freedom to

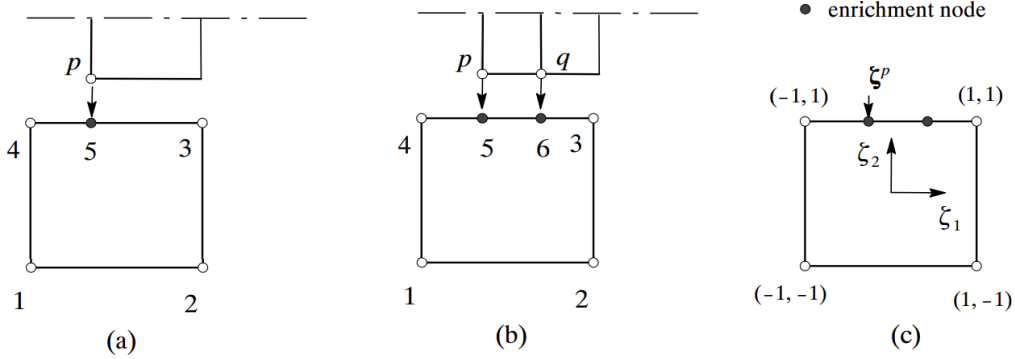


Fig. 2 Local enrichment of the interface element for the following cases: (a) Single node, (b) Multiple nodes, and (c) Added node reference in the parent domain (Haikal and Hjelmstad 2010)

enforce compatibility conditions at enrichment locations ( $\mathbf{u}^p = \mathbf{u}^5$ ,  $\mathbf{u}^q = \mathbf{u}^6$ ) without introducing bias or inducing over-constraint. Each enrichment increases the order of interpolation in the enriched element, and thus, while compatibility is enforced discretely at enrichment locations, differences in interpolation order between elements on opposing sides lead to a non-conforming displacement field along the interface. The enrichment applies only to the shape functions that are non-zero at the interface ( $N^3$  and  $N^4$  in the given case), and the order of interpolation along all other interfaces remains the same, thereby preserving the conformity of the mesh at these interfaces. Moreover, the nodal displacement continuity constraints can be accommodated automatically by the assembly procedure without the need for additional variables or Lagrange multipliers.

### 3.2 EDGA: Traction equilibrium

The goal of the DG-based stabilization procedure is to ensure a complete transfer of the traction field across the interface. The motivation behind the stabilization approach is based on the formulation of the coupled problem, as discussed in Section 2. As observed in Eq. (7), if the variational displacement field is continuous across the element boundaries, the interface term becomes a weak statement of equilibrium of tractions. When this condition is not met, equilibrium of tractions does not necessarily hold, and the presence of the interface term is a potential source of numerical instability.

In order to stabilize the solution and enforce traction continuity, the interface term in Eq. (9) is modified to include the weighted residual of interface traction equilibrium, yielding

$$I_* = \sum_e \int_{\Gamma_{e_*}^1} \boldsymbol{\sigma}^{1h} \mathbf{n}^1 \cdot \mathbf{w}^{1h} d\Gamma + \sum_e \int_{\Gamma_{e_*}^2} \boldsymbol{\sigma}^{2h} \mathbf{n}^2 \cdot \mathbf{w}^{2h} d\Gamma - \sum_e \int_{\Gamma_{e_*}^2} [\boldsymbol{\sigma}^{1h} \mathbf{n}^1 + \boldsymbol{\sigma}^{2h} \mathbf{n}^2] \cdot \mathbf{w}^{*h} d\Gamma \quad (13)$$

$$I_* = \sum_e \int_{\Gamma_{e_*}^1} \boldsymbol{\sigma}^{1h} \mathbf{n}^1 \cdot [\mathbf{w}^{1h} - \mathbf{w}^{*h}] d\Gamma + \sum_e \int_{\Gamma_{e_*}^2} \boldsymbol{\sigma}^{2h} \mathbf{n}^2 \cdot [\mathbf{w}^{2h} - \mathbf{w}^{*h}] d\Gamma$$

where  $\mathbf{w}^{*h}$  is chosen to be the average of the variational displacements along the interface  $\mathbf{w}^{*h} = (\mathbf{w}^{1h} + \mathbf{w}^{2h})/2$  to guarantee an unbiased method. Simplifying and rearranging the terms in the above equation, yields the following expression for interface terms

$$I_* = \sum_e \frac{1}{2} \int_{\Gamma_{e_*}^1} \boldsymbol{\sigma}^{1h} \mathbf{n}^1 \cdot [\mathbf{w}^{1h} - \mathbf{w}^{2h}] d\Gamma + \sum_e \frac{1}{2} \int_{\Gamma_{e_*}^2} \boldsymbol{\sigma}^{2h} \mathbf{n}^2 \cdot [\mathbf{w}^{2h} - \mathbf{w}^{1h}] d\Gamma \quad (14)$$

The interface term vanishes when the variational displacement field is conforming  $\mathbf{w}^{*h} = \mathbf{w}^{1h} = \mathbf{w}^{2h}$ , and the formulation reverts back to the standard continuous Galerkin method. The traction stabilization terms are based on local estimates of interface tractions, unlike DG formulations that typically employ numerical fluxes. This feature of the method is particularly relevant in the application of this approach within the realm of plasticity since interface tractions can be evaluated using any appropriate material law, including inelasticity.

#### 4. Material laws

In this paper, we implement the elasto-plastic constitutive models for rate-independent plasticity governed by the Von-Mises and Drucker-Prager yield criteria. Both models employ a decomposition of stress and strain tensors into volumetric and deviatoric parts as follows

$$\begin{aligned} \boldsymbol{\sigma} &= p \mathbf{I} + \boldsymbol{\tau} \\ \mathbf{E} &= \frac{1}{3} e \mathbf{I} + \boldsymbol{\varepsilon} \end{aligned} \quad (15)$$

In these equations  $\boldsymbol{\tau}$ ,  $\boldsymbol{\varepsilon}$  are the deviatoric parts of the Cauchy stress  $\boldsymbol{\sigma}$  and Lagrangian strain  $\mathbf{E}$  tensors, respectively,  $p \equiv \frac{1}{3} \text{tr}(\boldsymbol{\sigma})$  is the equivalent pressure, and  $e \equiv \text{tr}(\mathbf{E})$  is the volumetric rate of change. Assuming small deformations and an additive decomposition of the deviatoric strain tensor into elastic  $\boldsymbol{\varepsilon}^e$  and inelastic  $\boldsymbol{\varepsilon}^p$  components, the elasto-plastic constitutive equations can be expressed as follows

$$\begin{aligned} \boldsymbol{\tau} &= 2\mu \boldsymbol{\varepsilon}^e = 2\mu(\boldsymbol{\varepsilon} - \boldsymbol{\varepsilon}^p) \\ \boldsymbol{\sigma} &= p \mathbf{I} + \boldsymbol{\tau} = 3Ke \mathbf{I} + \boldsymbol{\tau} \end{aligned} \quad (16)$$

where  $K, \mu$  are the material bulk and shear moduli. The deviatoric stress component is governed by a yield function that determines the onset of plastic deformations

$$f(\boldsymbol{\tau}, \boldsymbol{\varepsilon}^p) \leq 0 \quad (17)$$

The elastic state occurs when  $f(\boldsymbol{\tau}, \boldsymbol{\varepsilon}^p) \leq 0$ , in which case no flow of plastic strains occurs  $\dot{\boldsymbol{\varepsilon}}^p = \mathbf{0}$ , while the inelastic state occurs when  $f(\boldsymbol{\tau}, \boldsymbol{\varepsilon}^p) > 0$  leading to a non-zero plastic strain rate  $\|\dot{\boldsymbol{\varepsilon}}^p\| > 0$  in the direction  $\mathbf{r}$ , and a return-mapping algorithm is activated to bring the deviatoric stress field back to the yield surface  $\dot{\boldsymbol{\varepsilon}}^p = \gamma \mathbf{r}$ , where  $\gamma > 0$  is the rate-independent consistency parameter.

This leads to the Kuhn-Tucker conditions for inelasticity

$$\gamma > 0, \quad f \leq 0, \quad \gamma f = 0. \quad (18)$$

In addition to the consistency condition  $\gamma \dot{f} = 0$ . These equations are integrated numerically

using the Backward Euler scheme to compute plastic strains  $\boldsymbol{\varepsilon}_{n+1}^p$  at each time step from previous values  $\boldsymbol{\varepsilon}_n^p$ , which are stored as internal variables at material integration points. We assume no kinematic or isotropic hardening.

#### 4.1 Von-mises plasticity

The Von-Mises yield criterion is typically used when yielding of materials depends only on the second deviatoric stress invariant  $J_2$ . Since the onset of plastic deformations is independent of the first stress invariant  $I_1 = \text{tr}(\boldsymbol{\sigma})$  this criterion is appropriate for the analysis of plastic deformations in ductile materials such as metals.

The Von-Mises yield surface is defined by the function

$$f(\boldsymbol{\sigma}, \boldsymbol{\varepsilon}^p) = \|\boldsymbol{\tau}\| - \tau_y \leq 0 \quad (19)$$

with  $\|\boldsymbol{\tau}\| = \sqrt{\boldsymbol{\tau} : \boldsymbol{\tau}}$  and  $\tau_y$  is typically a function of the equivalent plastic strain  $\|\boldsymbol{\varepsilon}^p\|$ . In the absence of hardening  $\tau_y = \sqrt{2/3} \sigma_y$ , where  $\sigma_y$  is the yield stress in uniaxial tension. When the yield surface is exceeded, plastic flow occurs in the direction  $\mathbf{r}$  such that  $\dot{\boldsymbol{\varepsilon}}_p = \gamma \mathbf{r}$ . It is often assumed that metals follow an associative flow rule such that  $\mathbf{r} = \frac{\partial f}{\partial \boldsymbol{\tau}} = \frac{\boldsymbol{\tau}}{\|\boldsymbol{\tau}\|}$ .

The governing equations for Von-Mises plasticity are typically integrated using the backward Euler scheme. The discretized equations, as well as derivations algorithmic consistent tangent  $\mathbb{D} = \frac{\partial \boldsymbol{\sigma}_{n+1}}{\partial \mathbf{E}_{n+1}}$  can be found in detail in Simo and Huges (1998).

#### 4.2 Drucker-prager plasticity

The Drucker-Prager yield criterion is an elastic-plastic two-parameter function that is frequently used due to its simplicity and applicability to materials such as soil and concrete. The Drucker-Prager model can be described as a smoothed Mohr-coulomb surface or as an extension of Von-Mises surface to account for the hydrostatic pressure  $p$ . It is expressed as

$$f(\boldsymbol{\sigma}, \boldsymbol{\varepsilon}^p) = \|\boldsymbol{\tau}\| + \alpha p - k \leq 0 \quad (20)$$

where  $\alpha$  is the frictional coefficient and  $k$  is the cohesion coefficient calculated as

$$\alpha = \frac{3 \tan \varphi}{\sqrt{(9 + 12 \tan^2 \varphi)}} \quad (21)$$

$$k = \frac{3c}{\sqrt{(9 + 12 \tan^2 \varphi)}} \quad (22)$$

with  $c$  and  $\varphi$  representing the cohesion and dilation angle, respectively. In this model, plastic flow follows a non-associative flow rule with

$$\mathbf{r} = \frac{\boldsymbol{\tau}}{\|\boldsymbol{\tau}\|} \neq \frac{\partial f}{\partial \boldsymbol{\tau}} \quad (23)$$

### 5. Numerical integration of material internal variables

The main challenge in extending the EDGA approach to materials with inelastic constitutive behavior is the issue of numerical integration. The EDGA enforces geometric compatibility along the interface by inserting a new node at contact locations, a process that may be repeated at multiple locations within a single element. Each enrichment in the element raises the order of interpolation in the element shape function associated with the nodes located on the non-conforming interface. Thus, the order of integration within the element has to be increased to accommodate the higher-order integrand.

In solids with elastic or hyper-elastic material behavior, increasing the order of the Gauss integration scheme can be accomplished by simply using a grid with more sampling material points. This process, however, could be problematic for the case of inelasticity. For history-dependent materials in which internal variables are accumulated at the Gauss points after each load increment, the computational history at the integration points before enrichment must be preserved. Since the process of optimizing integration point locations (and associated weights) within the Gauss quadrature rules yields different material point coordinates for each integration order, upgrading the integration rule for the purpose of accuracy leads to a loss of material data stored at existing material points.

In order to circumvent this issue, a progressive integration rule such as the Gauss-Kronrod quadrature can be used. The Gauss-Kronrod quadrature inherits Gauss point locations and provides an additional set of integration points interlaced between the original Gaussian quadrature. The derivation of the Gauss-Kronrod formula is similar to standard Gauss quadrature and the locations of the new points, as well as the new weights for existing Gauss and added Kronrod points are chosen to maximize accuracy. The difference in the integral values between the two sets can be used as an error estimate.

To illustrate the process of computing the Gauss-Kronrod integration points and weights, we consider a polynomial function  $f(x)$  that can be integrated accurately with a  $N$ -point Gauss quadrature. The order of integration is increased by adding  $N+1$  Kronrod points such that the resulting rule is of order  $(N+1)$ . The locations and weights of the additional integration points are computed through the following steps (Laurie 1997)

- First, we evaluating the integral using a  $N$ -point Gauss quadrature

$$\int_{-1}^1 f(x) dx = \sum_{k=1}^N w_k f(x_k) \tag{24}$$

where  $w_k$  and  $x_k$  are the locations and weights of the original Gauss quadrature

- Next, we re-evaluate the integral using a  $2N+1$  Gauss-Kronrod quadrature. The locations of the original  $N$  Gauss points are recycled. The locations and corresponding weights of  $N+1$  additional points are calculated, as well as weights associated with the original  $N$  Gauss points such that

$$\int_{-1}^1 f(\mathbf{x}) dx = \sum_{k=1}^N z_k f(x_k) + \sum_{j=1}^{N+1} m_j f(y_j) \tag{25}$$

While the locations  $x_k$  are imported from the original Gauss quadrature, the remaining  $3N+2$  parameters  $z_k$ ,  $m_j$ , and  $y_j$  are chosen such that Eq. (25) is integrated with maximum degree of

accuracy.

### 5.1 Application to EDGA

Consider the enriched Q4 element shown in Fig. 3. We assume an enrichment of the top surface  $\zeta_2 = 1$ , which introduces a quadratic term in  $\zeta_1$  in the element shape functions associated with the nodes located on this interface, while the order of interpolation with respect to  $\zeta_2$  remains the same.

$$\tilde{N}^p(\boldsymbol{\zeta}, \boldsymbol{\zeta}^p) = \frac{1}{2}(\zeta_2 + 1) \frac{(\zeta_1 + 1)(\zeta_1 - 1)}{(\zeta_1^p + 1)(\zeta_1^p - 1)} \quad (26)$$

$$\tilde{N}^\alpha(\boldsymbol{\zeta}, \boldsymbol{\zeta}^p) = N_{Q4}^\alpha(\boldsymbol{\zeta}) - N_{Q4}^\alpha(\boldsymbol{\zeta}^p) \tilde{N}^p(\boldsymbol{\zeta}, \boldsymbol{\zeta}^p) \quad (27)$$

Therefore, for the element to be integrated properly, the integration rule order has to be increased in the direction of  $\zeta_1$ . For the use of this element in non-conforming mesh simulations, two different sets of Gauss-Kronrod integration points are needed. The first set is used inside the element as illustrated in Fig. 3, where the stresses and plastic strains are computed to find the internal forces and tangential stiffness of the element. In addition, Gauss-Kronrod integration points are needed on the interface as illustrated in Fig. 4, to be used for the stabilization terms, where the stresses and plastic strain are computed as well.

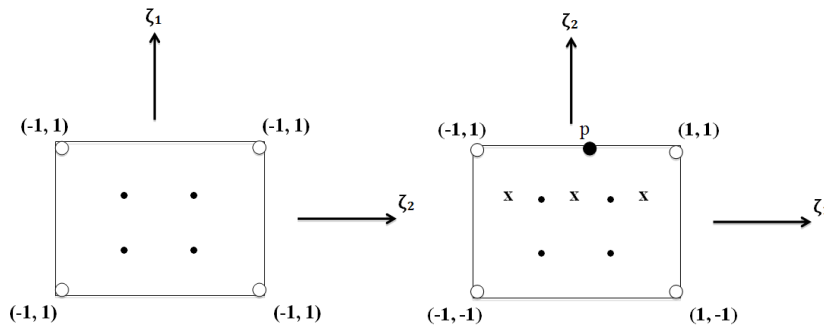


Fig. 3 Q4 Element with Gauss quadrature integration points inside (Left) and the enriched element with Gauss-Kronrod integration points (Right)

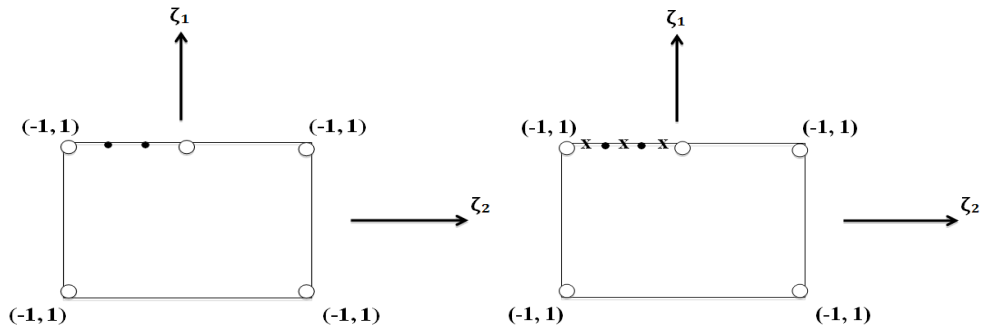


Fig. 4 Q4 Element with Gauss Quadrature Integration Points at the Interface (Left) and the Enriched Element with Gauss-Kronrod Integration Points (Right)

The Kronrod points are added such that integration order is increased in one spatial direction, as required by the enrichment-induced higher interpolation ( $\zeta_1$  in the above example), without undue expense in directions where the original quadrature is sufficient to integrate the element adequately. Furthermore, the additional integration points within the element are chosen to increase integration order closer to the interface, where the higher-order shape functions are expected to be non-zero (Fig. 3). The added material points on the interface (Fig. 4) enable a more accurate evaluation of interface tractions, therefore ensuring the smooth transfer of stress fields and the effectiveness of interface-targeted enrichments of interface variables through the EDGA.

Table 1 lists the values of the locations and weights for the Gauss-Kronrod integration points  $i$  including the Gauss quadrature for exact integration of a cubic function  $N=2$  for the example shown in Fig. 3.

Table 1 Gauss-Kronrod Quadrature Locations and Weights for  $N=2$

$i$	Kronrod $\zeta_1$	Kronrod $\zeta_2$	Kronrod $w_i$	Gauss $w_i$
1	-0.9258200977	0.57735026918	0.19797979798	---
2	-0.57735026918	0.57735026918	0.49090909090	1
3	0	0.57735026918	0.62222222222	---
4	0.57735026918	0.57735026918	0.49090909090	1
5	0.9258200977	0.57735026918	0.19797979798	---

The values of history-dependent variables at original Gauss points are preserved throughout the analysis. When enrichment occurs and Gauss-Kronrod integration points are added, we compute the values of plastic internal variables at the new integration points by interpolation/extrapolation from the existing values using the element shape functions, as shown in Fig. 5.

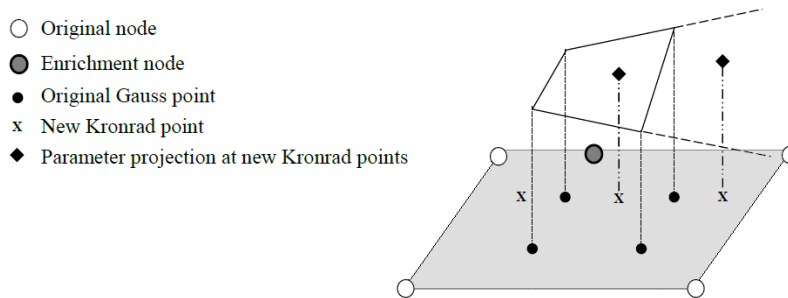


Fig. 5 Interpolation of material internal parameters at Kronrod points

## 6. Results and discussion

### 6.1 Example 1

In this example, we test the formulation's ability to pass the patch test with a non-conforming

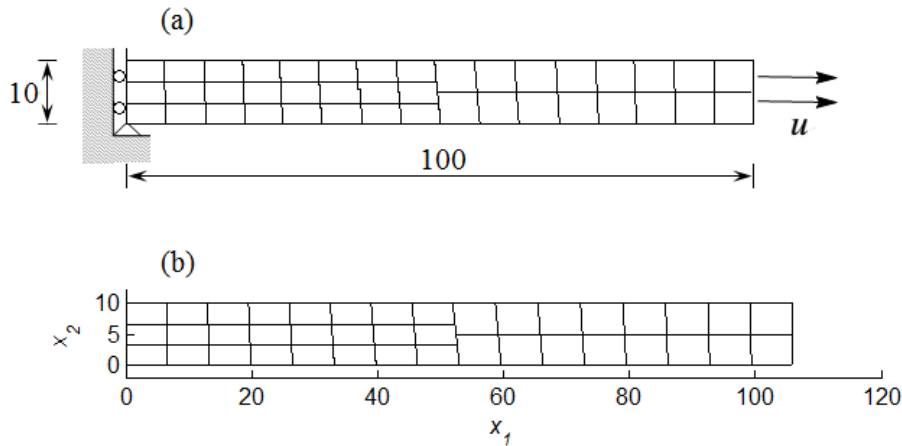


Fig. 6 Bar under uniaxial tension (a) configuration and (b) deflected shape at  $u = 1.5$  (with magnification factor of 2)

mesh discretization in the presence of plasticity. The bar shown in Fig. 6 is of length  $L = 100$  and has a cross section of dimensions  $10 \times 1$ . The bar is supported at its left end and subjected to a constant displacement field at its right edge, with material properties  $E = 30,000$ ,  $\nu = 0$  and  $\sigma_y = 60$  as measured in a uniaxial tension test. We assume plane stress conditions and the Von-Mises material law with no isotropic or kinematic hardening.

We discretize the bar with a non-conforming mesh of bilinear (Q4) elements, as shown in Fig. 6(a), with an inclined interface located at a distance of 50 from the left support. The inclined interface serves to produce elements with non-constant Jacobian, with a more refined mesh in the left partition. Yielding is expected to occur at a displacement value of  $u = 0.2$ , which corresponds to a uniaxial strain of 0.2%. We run the analysis over 30 steps with increments  $\Delta u = 0.2$  to test the ability of the formulation to preserve material history (plastic strains) well beyond initial yield.

As expected, yielding occurred at step 5 when the applied displacement exceeded 0.2. Fig. 6(b) shows the deflected shape at the end of the simulation, at  $u = 1.5$ , in which the displacements were magnified by a factor of 2 for clarity. The deflected shape displays a linear displacement field, with values increasing at a constant rate from the left support, and with full compatibility along the non-conforming interface.

Fig. 7 displays the stress fields at  $u = 1.5$  and clearly show the expected solution, with a constant axial stress distribution in the horizontal direction equal to the yield stress, and zero vertical axial and shear stresses throughout the domain. The stress fields are smooth and exhibit no oscillations at the non-conforming interface, which reflects the accuracy of internal material history at the Gauss-Kronrod integration points along the interface.

These results show that the formulation is capable of transferring complete stress fields and preserve material history accurately in the presence of relatively large plastic deformations.

## 6.2 Example 2

This example applies the pressure-dependent Drucker-Prager model to a domain discretized with mixed quadratic (Q8) and bilinear (Q4) elements. The square  $1 \times 1m$  domain shown in Fig. 8

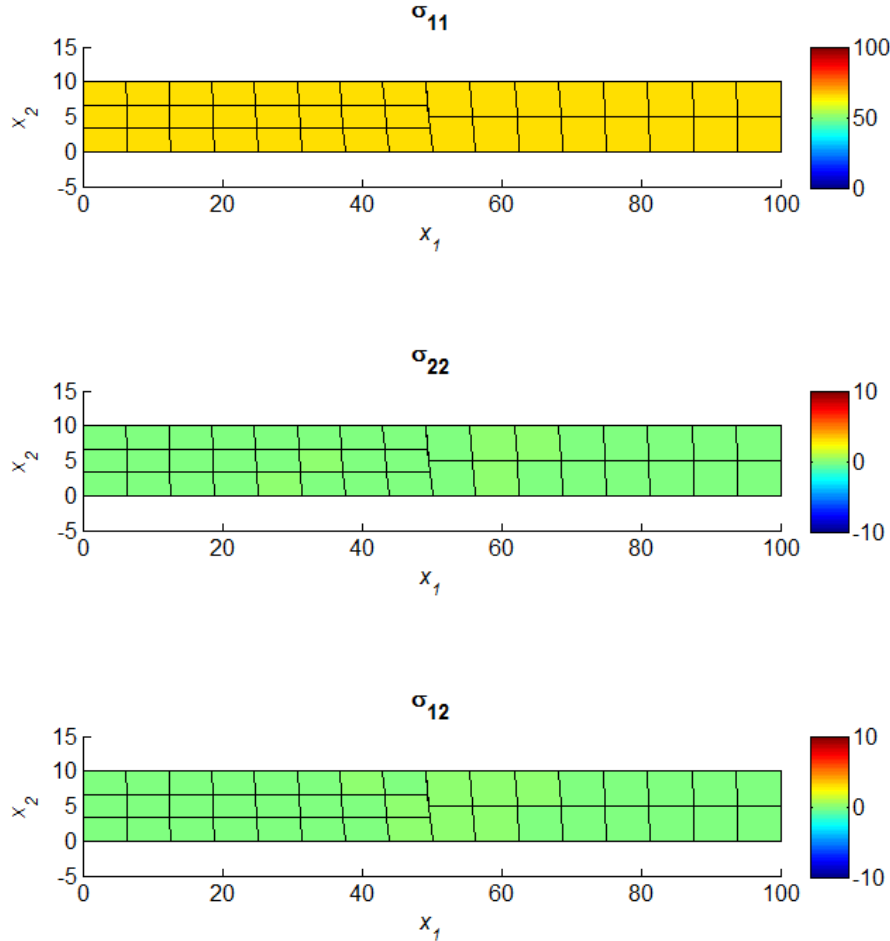


Fig. 7 Stress distribution at  $u = 1.5$ , axial strain 0.2%

is supported vertically at its bottom edge and horizontally along its left edge. A constant displacement field  $u_1$  is applied at the right domain edge while the top edge is subjected to a vertical displacement  $u_2$ . The domain is under plane strain conditions and discretized with a mixed mesh of Q4 and Q8 elements, thereby creating a variety of non-conforming interfaces with different orders of interpolation in the primary field. This configuration is chosen to test the formulation's ability to adapt to different element configurations and interpolation orders. The material properties in the domain are assumed to be  $E = 10,000$  Kpa,  $\nu = 0.3$ ,  $k = 1.8$  Kpa and  $\alpha = 0.1$ , which corresponds to a cohesion of  $c = 2$  Kpa and dilation angle of  $20^\circ$ .

According to the Drucker-Prager model, a compressive pressure leads to an increase in the size of the yield surface, while tensile stress produces the opposite effect. We apply the model under both conditions to test the ability of the interface formulation to maintain the accuracy of the stress and plastic strain fields under varying pressure fields.

Fig. 9 shows the obtained deflected shape when a constant (a) compressive and (b) tensile fields are applied to the sample with maximum displacement of  $u_1 = u_2 = 0.6$  mm (magnified by

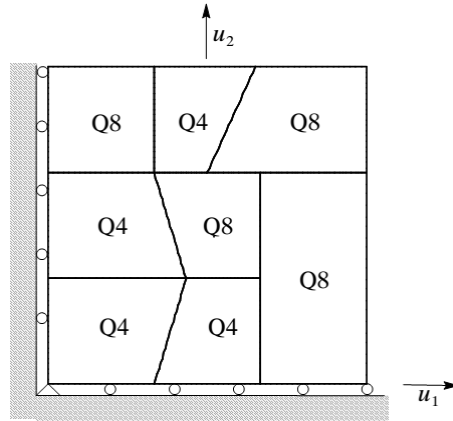


Fig. 8 Square domain discretized with mixed elements in plane strain conditions

a factor of 100 in the figure). The shapes reflect consistent deformations with intensity increasing linearly away from the support. The non-conforming interfaces are modeled accurately with perfect displacement compatibility along interfaces connecting elements with different orders of interpolation.

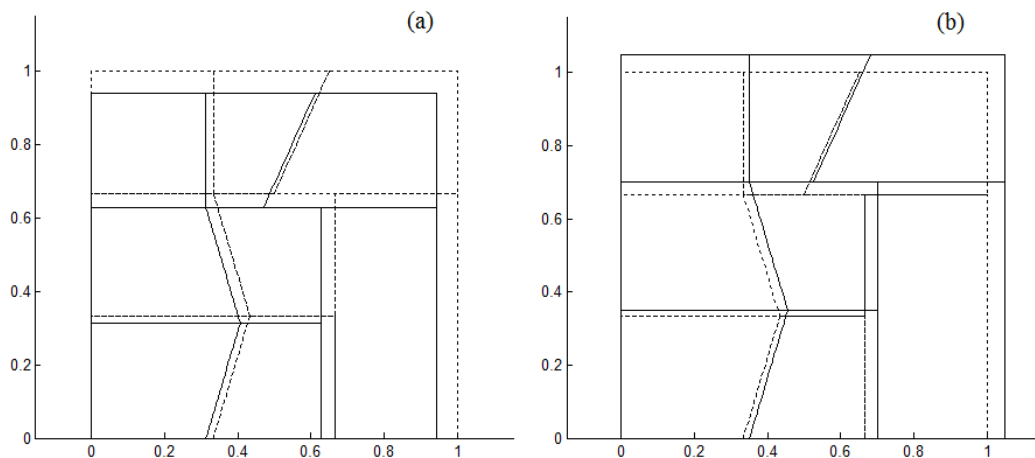


Fig. 9 Deformed shape under uniform (a) compression and, (b) tension (displacements magnified by 100)

The stress fields are shown in Fig. 10 for compression (a) and tension (b) cases. The results also show constant stress fields with no oscillations across the non-conforming interfaces. No shear stresses are detected, as expected, and yield stress values show the influence of hydrostatic pressure on increasing and decreasing material strength in compression and tension, respectively.

Fig. 11 shows variations in axial stress with increasing applied strain for different dilation angles, both in tension and compression. It can be seen from this figure that increasing the dilation angle leads to a higher strength, and delayed initiation of plasticity when the sample is in

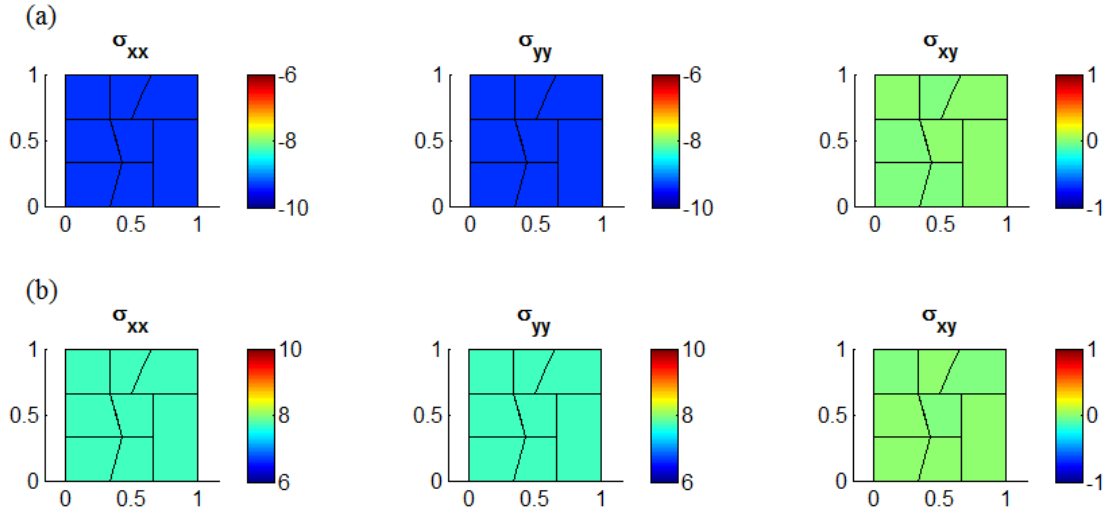


Fig. 10 Stress distribution under uniform (a) compression and, (b) tension

compression, while a higher dilation angle causes early yielding in the sample under tension. These properties are expected with the Drucker-Prager model, and we therefore conclude that the interface formulation leads to accurate stress fields with smooth traces on non-conforming interfaces.

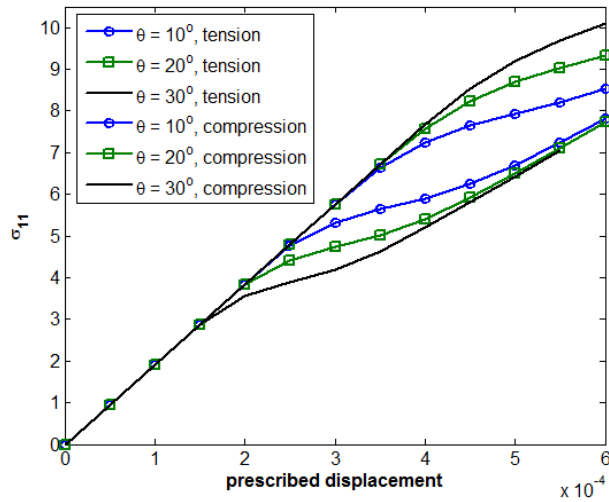


Fig. 11 Stress evolution with prescribed displacement for varying cohesion angle and loading conditions

### 6.3 Example 3

In this example, we test the performance of the proposed formulations under non-homogeneous loading conditions. The beam shown in Fig. 12 is fixed at both ends and subjected to an

incrementally-increasing distributed load  $q$ . The beam is of length 100, height 10, and unit thickness and is assumed to be loaded in plane stress conditions. We assume a Von-Mises material model with material parameters  $E = 29,000$ ,  $\nu = 0$  and yield strength  $\sigma_y = 60$ . Plastic hinges are expected to first occur at the fixed ends at a value of  $q = 1.2$ , with plastic deformations propagating to other parts of the beam with increasing load. Failure is expected to occur at  $q = 3$  with the formation of a third plastic hinge at the center of the beam. We discretize the beam with a mesh of Q8 elements, with a finer mesh at locations where concentration of plastic deformations is expected to produce plastic hinges at the ends and center of the beam.

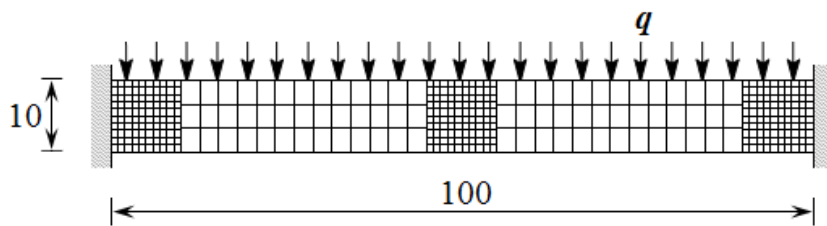


Fig. 12 Beam fixed at both ends under constant load: Non-conforming discretization with Q8 elements

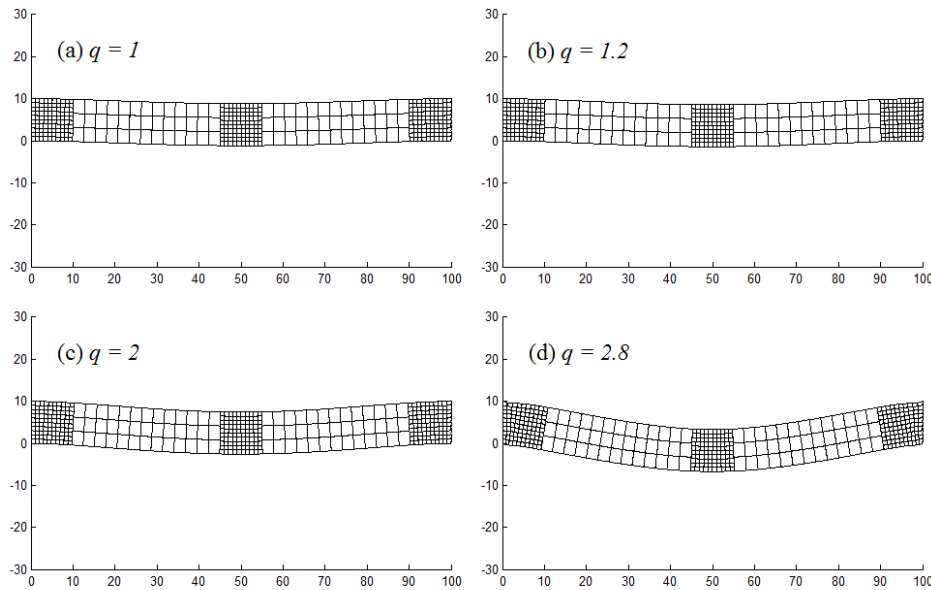


Fig. 13 Deflected shape at varying load levels (a) right before and (b) right after first yield, (c) with advanced plastic deformations and (d) right before failure (displacements magnified by 100)

Fig. 13 shows the beam deformation with increased applied load. We can see from this figure that the onset of plastic deformations at  $q = 1.2$  does not lead to a noticeable increase in beam deflections. With increased load values, however, the concentration of high deformation gradients at beam ends is obvious, as can be seen in Fig. 13(d).

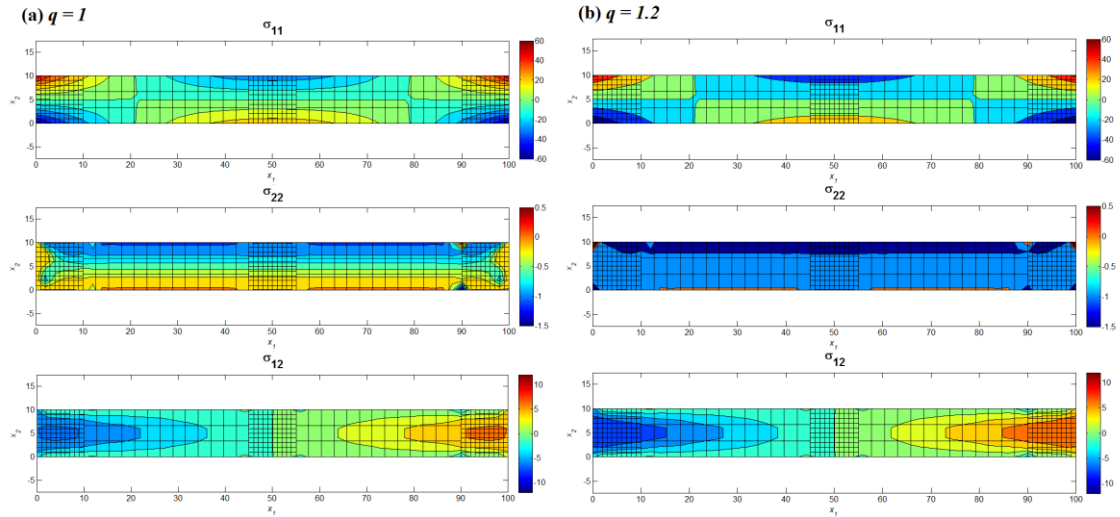


Fig. 14 Stress fields at varying load levels (a) right before and (b) right after first yield

The stress profiles are shown in Fig. 14 at load levels (a) before and (b) after first yield occurs at  $q = 1.2$ . While axial and shear stresses in Fig. 14 (a) show the expected pattern for bending-dominated problems, stress profiles change significantly with the onset of plasticity, with increasing values in other parts of the domain. Despite the presence of four non-conforming interfaces, the stress fields shown in Fig. 14 are in good agreement with the stresses obtained using a much refined conforming mesh, as shown in Fig. 15, both before (a) and after (b) the onset of plasticity.

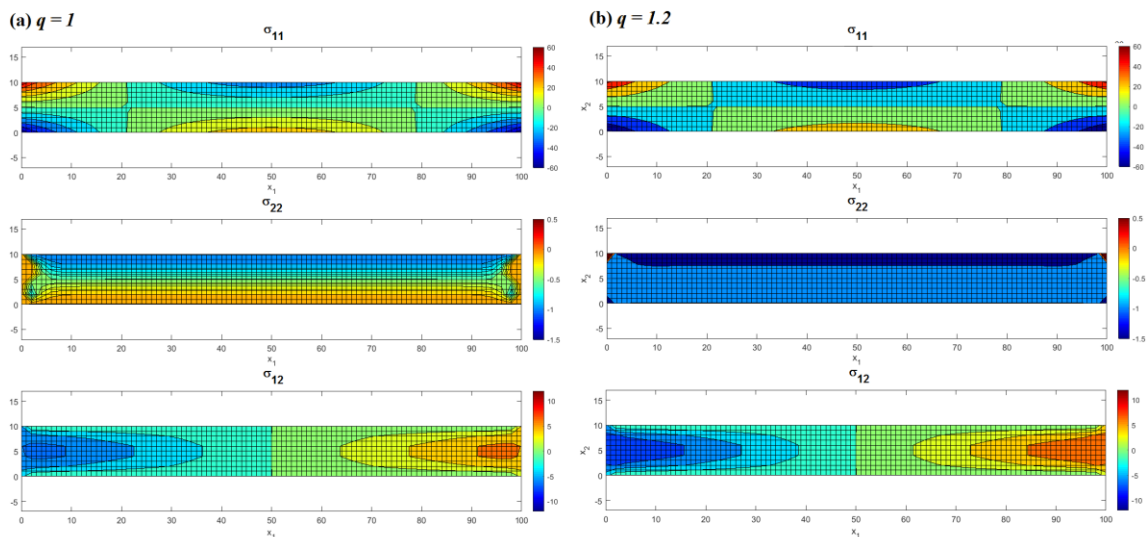


Fig. 15 Stress fields at varying load levels (a) right before and (b) right after first yield, conforming mesh

The stress redistribution becomes more obvious with increasing load levels, as shown in Fig. 16, leading to almost constant moments right before total failure, as shown in Fig. 16(b). At all load levels shown in Figs. 14 and 16, the stress transfer is smooth across all non-conforming interfaces, and the computed values agree with predicted values, which reflects the accuracy in material history within each element and along all non-conforming interfaces.

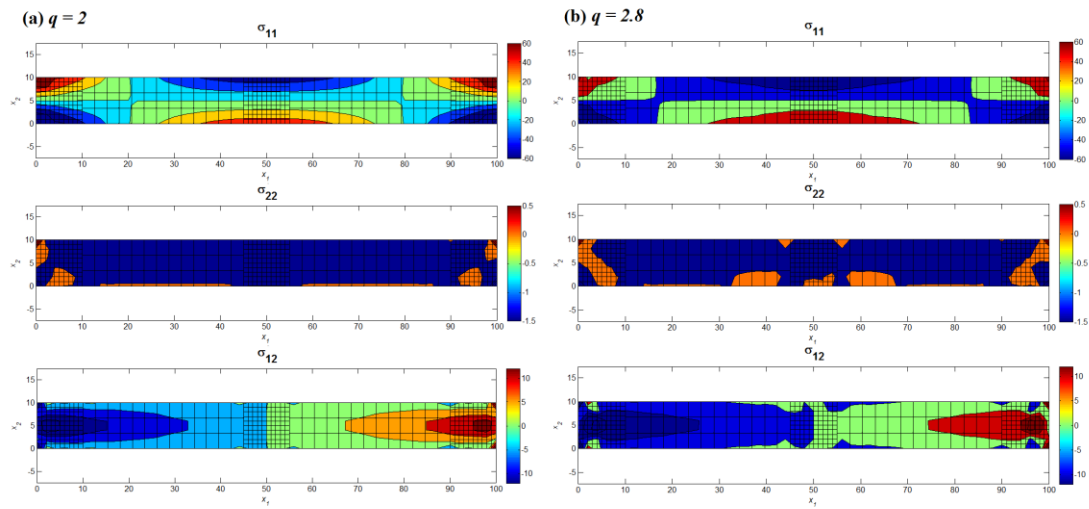


Fig. 16 Stress fields at varying load levels (a) advanced plastic deformations and (b) right before failure

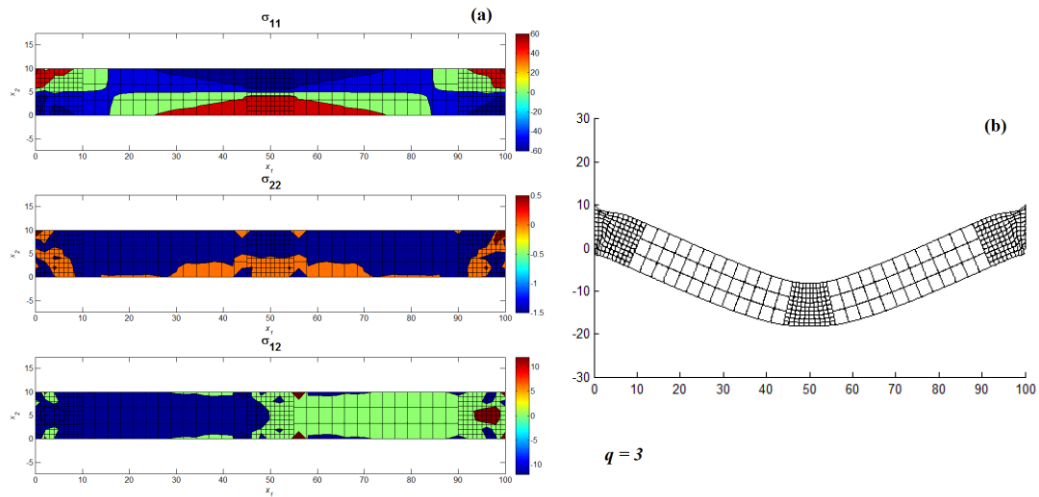


Fig. 17(a) Stress fields and (b) deflected shape at failure

Fig. 17 shows the stress profiles and deflected shape at failure for  $q=3$ , which also display accurate values and smooth stress profiles. The formulation's ability to deal with high deformation gradients and stress concentration is demonstrated effectively.

## 7. Conclusions

In this paper, we have presented a primal formulation for the coupling of non-conforming meshes in solids with inelastic behavior governed by the Von-Mises and Drucker-Prager material models. The proposed formulation is based on the Enriched Discontinuous Galerkin Approach (EDGA) for the coupling of Non-Conforming Meshes (Haikal and Hjelmstad 2010). The EDGA introduces a nodal enrichment that transforms displacement compatibility conditions into node-to-node constraints, therefore adding a higher order term to the element shape functions associated with the nodes located on the non-conforming interface. This requires an increase in the integration rule in the enrichment direction. A progressive integration rule (Gauss-Kronrod quadrature) is used to preserve the strain rates and load history. The progressive rule provides an additional set of integration points interlaced between the original Gaussian quadrature, such that the values of the plastic variables from the previous iterations are preserved at Gauss quadrature integration points. In the presence of enrichments Gauss-Kronrod integration points are activated, and the values of the plastic variables at the new integration points are created by interpolation/extrapolation from the existing values. The resulting formulation is consistent with the traditional Galerkin formulation and provides targeted interface enrichment fields that can effectively capture material history and produce a smooth transfer of stress fields on non-conforming finite element interfaces.

## References

- Arnold, D.N., Brezzi, F., Cockburn, B. and Marini, L.D. (2002), "Unified analysis of discontinuous Galerkin methods for elliptic problems", *SIAM J. Numer. Anal.*, **39**(5), 1749-1779.
- Bavestrello, H., Avery, P. and Farhat, C. (2007), "Incorporation of linear multipoint constraints in substructure based iterative solvers. Part II: Blending FETI-DP and mortar methods and assembling floating substructures", *Comput. Meth. Appl. Mech. Eng.*, **196**, 1347-1368.
- Bayat, H., Kramer, J., Wunderlich, L., Wulfinghoff, S., Wohlmuth, B., Resse, S. and Wieners, C. (2018), "Numerical evaluation of discontinuous and nonconforming finite element methods in nonlinear solid mechanics," *Comput. Mech.*, 1-15.
- Becker, R., Hansbo, P. and Stenberg, R. (2003), "A finite element method for domain decomposition with non-matching grids", *Math. Modell. Numer. Anal.*, **37**(2), 209-225.
- Belgacem, F.B., Hild, P. and Laborde, P. (1999), "Extension of the mortar finite element method to a variational inequality modeling unilateral contact", *Math. Mod. Meth. Appl. Sci.*, **9**(2), 287-303.
- Bernardi, C., Maday, Y. and Patera, A.T. (1992), "A new nonconforming approach to domain decomposition: The mortar element method", *Nonlin. Part. Different. Equat. Their Appl.*, 13-51.
- Bernardi, C., Rebello, C., Vera, C. and Coronil, C. (2009), "A posteriori error analysis for two non-overlapping domain decomposition techniques", *Comput. Meth. Appl. Mech. Eng.*, **59**(6), 1214-1236.
- Bernardi, C., Rebello, T.C. and Vera, E.C. (2008), "A FETI method with a mesh independent condition number for the iteration matrix", *Comput. Meth. Appl. Mech. Eng.*, **197**(13-16), 1410-1429.
- Bitencourt, L.A.G., Jr, Manzoli, O.L., Prazeres, P.G.C., Rodrigues, E.A. and Bittencourt, T.N. (2015), "A coupling technique for non-matching finite element meshes", *Comput. Meth. Appl. Mech. Eng.*, **290**, 19-44.
- Brezzi, F. and Fortin, M. (1991), *Mixed and Hybrid Finite Element Methods*, Springer Series in Computational Mathematics.
- Di Pietro, D.A. and Nicaise, S. (2013), "A locking-free discontinuous Galerkin method for linear elasticity in locally nearly incompressible heterogeneous media", *Appl. Numer. Math.*, **63**, 105-116.

- Dickopf, T. and Krause, R. (2009), "Efficient simulation of multi-body contact problems on complex geometries: A flexible decomposition approach using constrained minimization", *Int. J. Numer. Meth. Eng.*, **77**(13), 1834-1862.
- Dolbow, J.E. and Harari, I. (2009), "An efficient finite element method for embedded interface problems", *Int. J. Numer. Meth. Eng.*, **78**(2), 229-252.
- Farhat, C. (1991), "A method for finite element tearing and interconnecting and its parallel solution algorithm", *Int. J. Numer. Meth. Eng.*, **32**(6), 1205-1227.
- Farhat, C., Lacour, C. and Rixen, D. (2007), "Incorporation of linear multipoint constraints in substructure based iterative solvers. Part I: A numerically scalable algorithm", *Int. J. Numer. Meth. Eng.*, **43**(6), 997-1016.
- Fischer, K.A. and Wriggers, P. (2005), "Frictionless 2D contact formulations for finite deformations based on the mortar method", *Comput. Mech.*, **36**(3), 226-244.
- Grieshaber, B., McBride, A. and Reddy, B. (2015), "Uniformly convergent interior penalty methods using multilinear approximations for problems in elasticity", *SIAM J. Numer. Anal.*, **53**(5), 2255-2278.
- Haikal, G. and Hjelmstad, K.D. (2010), "An enriched discontinuous Galerkin formulation for the coupling of non-conforming meshes", *Fin. Elem. Anal. Des.*, **46**(6), 496-503.
- Haikal, G. (2009), "A stabilized finite element formulation of non-smooth contact", Ph.D. Dissertation, University of Illinois-Urbana Champaign, Illinois, U.S.A.
- Hansbo, A. and Hansbo, P. (2002), "An unfitted finite element method, based on Nitsche's method, for elliptic interface problems", *Comput. Meth. Appl. Mech. Eng.*, **191**(47-48), 5537-5552.
- Hansbo, P. and Larsson, F. (2016) "The nonconforming linear strain tetrahedron for a large deformation elasticity problem", *Computat. Mech.*, **58**(6), 929-935.
- Hansbo, P., Lovadina, C., Perugia, I. and Angalli, G. (2005), "A lagrange multiplier method for the finite element solution of elliptic interface problems using non-matching meshes", *Numeris. Mathemat.*, **100**(1), 91-115.
- Jin, S., Sohn, D., Lim, J.H. and Im, S. (2015), "A node-to-node scheme with the aid of variable-node elements for elasto-plastic contact analysis", *Int. J. Numer. Meth. Eng.*, **102**(12), 1761-1783.
- Kim, H.G. (2002), "Interface element method (IEM) for a partitioned system with non-matching interfaces", *Comput. Meth. Appl. Mech. Eng.*, **191**(29-30), 3165-3194.
- Kim, H.G. (2003), "Interface element method: Treatment of non-matching nodes at the ends of interfaces between partitioned domains", *Comput. Meth. Appl. Mech. Eng.*, **192**(15), 1841-1858.
- Laurie, D. (1997), "Calculation of gauss-kronrod quadrature rules", *Math. Comput. Am. Math. Soc.*, **66**(219), 1133-1145.
- Le Tallec, P. and Sassi, T. (1995) "Domain decomposition with nonmatching grids: Augmented lagrangian approach", *Math. Comput.*, **64**(212), 1367-1396.
- Liu, R., Wheeler, M.F. and Yotov, I. (2013), "On the spatial formulation of discontinuous Galerkin methods for finite elastoplasticity", *Comput. Meth. Appl. Mech. Eng.*, **253**, 219-236.
- Liu, R., Wheeler, M. and Dawson, C. (2009), "A three-dimensional nodal-based implementation of a family of discontinuous Galerkin methods for elasticity problems", *Comput. Struct.*, **87**(3-4), 141-150.
- Lloberas-Valls, O., Cafiero, M., Cante, J., Ferrer, A. and Oliver, J. (2017), "The domain interface method in non-conforming domain decomposition multifield problems", *Comput. Mech.*, **59**(4), 579-610.
- Masud, A., Truster, T. and Bergman, L.A. (2012), "A unified formulation for interface coupling and frictional contact modeling with embedded error estimation", *Int. J. Numer. Meth. Eng.*, **92**(2), 144-177.
- Montero, J. and Haikal, G. (2018), "Modeling beam-solid finite element interfaces: A stabilized formulation for contact and coupled systems", *Int. J. Appl. Mech., Imper. Colleg. Press*, **10**(9), 1850095.
- Nitsche, J. (1971), "Über ein variationsprinzip zur lösung von dirichlet problemen bei verwendung von teilträumen, die keinen randbedingungen unterworfen sind", *Abhandlungen in der Mathematik an der Universität Hamburg*, **36**(1), 9-15.
- Popp, A. and Wall, W.A. (2014), "Dual mortar methods for computational contact mechanics-overview and

- recent developments”, *GAMM-Mitteilungen*, **37**(1), 66-84.
- Puso, M.A. and Laursen, T.A. (2004), “A mortar segment-to-segment contact method for large deformation solid mechanics”, *Comput. Meth. Appl. Mech. Eng.*, **193**(6-8), 601-629.
- Rivière, B., Wheeler, M.F. and Girault, V. (1999), “Improved energy estimates for interior penalty, constrained and discontinuous Galerkin methods for elliptic problems I”, *Comput. Geosci.*, **3**(3-4), 337-360.
- Sanders, J., Dolbow, J.E. and Laursen, T.A. (2009), “On methods for stabilizing constraints over enriched interfaces in elasticity”, *Int. J. Numer. Meth. Eng.*, **78**(9), 1009-1036.
- Simo, J.C. and Hughes, T.J.R. (1998), *Computational Inelasticity*, Springer.
- Solberg, J.M. and Papadopoulos, P. (2005), “An analysis of dual formulations for the finite element solution of two-body contact problems”, *Comput. Meth. Appl. Mech. Eng.*, **194**(25-26), 2734-2780.
- Solberg, J.M., Jones, R.E. and Papadopoulos, P. (2007), “A family of simple two-pass dual formulations for the finite element solution of contact problems”, *Comput. Meth. Appl. Mech. Eng.*, **196**(4-6), 782-802.
- Wihler, T. (2006), “Locking-free adaptive discontinuous Galerkin FEM for linear elasticity problems”, *Math. Comput.*, **75**(255), 1087-1102.
- Wohlmuth, B.I. (2000), “A mortar finite element method using dual spaces for the lagrange multiplier”, *SIAM J. Numer. Anal.*, **38**(3), 989-1012.
- Wriggers, P., Rust, W.T. and Reddy, B.D. (2016), “A virtual element method for contact”, *Comput. Mech.*, **58**(6), 1039-1050.
- Yang, B., Laursen, T.A. and Xiaonong, M. (2005), “Two-dimensional mortar contact methods for large deformation frictional sliding”, *Int. J. Numer. Meth. Eng.*, **62**(9), 1183-1225.